ACSNANO
www.acsnano.org
ARTICLE

Tumor-Triggered Geometrical Shape Switch of Chimeric Peptide for Enhanced *in Vivo* Tumor Internalization and Photodynamic Therapy

Kai Han,[†] Jin Zhang,[†] Weiyun Zhang,[†] Shibo Wang,[‡] Luming Xu,[§] Chi Zhang,[‡] Xianzheng Zhang,[‡] and Heyou Han*,[†]

[†]State Key Laboratory of Agricultural Microbiology, College of Science, Huazhong Agricultural University, Wuhan 430070, China
[‡]Key Laboratory of Biomedical Polymers of Ministry of Education & Department of Chemistry, Wuhan University, Wuhan 430072, China
[§]China Research Center for Tissue Engineering and Regenerative Medicine, Union Hospital, Tongji Medical College, Huazhong University of Science and Technology, Wuhan 430022, China

Supporting Information

ABSTRACT: **Geometrical shape of nanoparticles plays an important role in cellular internalization. However, the applicability in tumor selective therapeutics is still scarcely reported. In this article, we designed a tumor extracellular acidity-responsive chimeric peptide with geometrical shape switch for enhanced tumor internalization and photodynamic therapy. This chimeric peptide could self-assemble into spherical nanoparticles at physiological condition. While at tumor extracellular acidic microenvironment, chimeric peptide underwent detachment of acidity-sensitive 2,3-dimethylmaleic anhydride groups. The subsequent recovery of ionic complementarity between chimeric peptides resulted in formation of rod-like nanoparticles. Both *in vitro* and *in vivo* studies demonstrated that this acidity-triggered geometrical shape switch endowed chimeric peptide with accelerated internalization in tumor cells, prolonged accumulation in tumor tissue, enhanced photodynamic therapy, and minimal side effects. Our results suggested that fusing tumor microenvironment with geometrical shape switch should be a promising strategy for targeted drug delivery.**

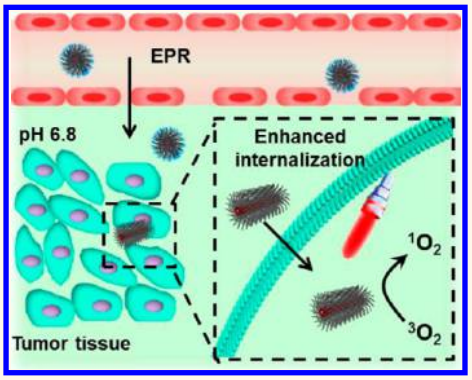

KEYWORDS: *geometrical shape switch, acidity responsive, chimeric peptide, enhanced cellular internalization, photodynamic therapy*

Nanoparticles have garnered considerable attention in transporting drugs to tumor tissue with controlled drug release and improved bioactivity.[1−4] Despite the great success of nanoparticles in tumor therapy, these nanoparticles still face the inherent restriction of poor tumor target during circulation, which decreases therapeutic efficacy and results in severe toxic side effects inevitably.[5,6] A promising approach to solve this limitation is to develop tumor microenvironment responsive nanoparticles.[7−11] Generally, tumor microenvironment can mediate specific breakage of certain chemical structure. Physicochemical parameters including hydrodynamic size, rigidity or, surface chemistry can be precisely manipulated during this process, leading to actively or passively target to tumor tissue with improved cellular internalization.[12−15] However, among these physicochemical parameters, geometrical shape of nanoparticles has not received enough attention to date, partly because of the ease of making spherical nanoparticles and the challenge of designing nonspherical nanoparticles.[16−19] Actually, some microorganisms in nature with nonspherical shape, such as polygonal adenovirus or rod bacteria, exhibit powerful infection capability to animal cells.[20] Motivated by this phenomenon, some pioneering studies have systematically evaluated the influence mode of cellular internalization among nanoparticles with various shapes.[21−23] Zhou et al. demonstrated that rod-like micelles exhibited accelerated cellular internalization than sphere-shaped micelles.[24] He et al. revealed that appropriate increase of aspect ratio would facilitate the cellular uptake of mesoporous silica nanoparticles.[25] Herrmann et al. found that rod-like polymeric particles could be taken up more efficiently than their spherical counter parts.[26] Unfortunately, most of current work focus on revealing the potential effects of geometrical shape on the rate of cellular uptake and body distribution. These optimized nanoparticles with given geometrical shape can exhibit accelerated cellular internalization in cells, but they always fail

Received: January 11, 2017
Accepted: March 15, 2017
Published: March 15, 2017

DOI: 10.1021/acsnano.7b00216
ACS Nano XXXX, XXX, XXX−XXX

to discern tumor cells from the healthy ones efficiently. It can be imagined that if tumor microenvironment can trigger certain geometrical shape switch of nanoparticles, a promising tumor-targeted drug delivery system fusing tumor responsiveness into accelerated cellular internalization could be expected.

Aiming at this goal, in this work, we reported a chimeric peptide with tumor extracellular acidity-responsive sphere-to-rod shape switch for enhanced cellular internalization and photodynamic therapy (PDT) in tumor. Herein, tumor extracellular acidity was chosen as a broad-spectrum stimulus. Different from some enzymes or receptors that only overexpressed in certain tumors, almost all types of tumors exhibit mild acidity due to the high rate of glycolysis and subsequent production of lactic acid by tumor cells.[27−29] The chimeric peptide was fabricated using (i) an alkylated photosensitizer protoporphyrin IX (PpIX) for PDT, (ii) dimethylmaleic anhydride (DMA) modified (Ala-Glu-Ala-Glu-Ala-Lys-Ala-Lys)$_2$ (AEAEAKAKAEAEAKAK) peptide sequence for self-assembly. The obtained peptide was designated as PEAK-DMA. It was known that AEAEAKAKAEAEAKAK peptide sequence has two surfaces in neutral solution, i.e., the polar surface owns alternatively charged ionic side chains (Glu and Lys) and the nonpolar surface owns alanines (Ala). The ionic complementarity, together with hydrogen bonding, hydrophobicity, and van der Waals interactions, could drive the self-assembly of PpIX-Ahx-AEAEAKAKAEAEAKAK (denoted as PEAK).[30,31] As shown in Figure 1, PEAK-DMA could self-assemble into spherical nanoparticles during blood circulation due to the introduction of acidity liable DMA groups, which prevented electrostatic interaction between PEAK.[32,33] Once arriving at tumor region, tumor extracellular acidity initiated detachment of DMA groups. Recovered ionic complementarity mediated the formation of short rod-like nanoparticles. This sphere-to-rod switch improved the internalization of chimeric peptide in tumor, achieving enhanced PDT efficacy and negligible side effects both *in vitro* and *in vivo*.

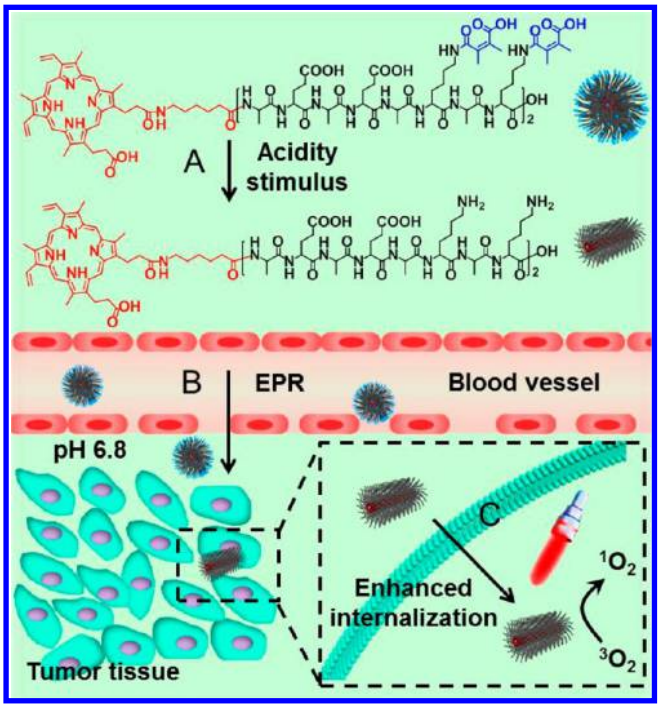

Figure 1. Schematic illustration of acidity-triggered geometrical shape switch and enhanced PDT: (A) mechanism of detachment of DMA under acidity stimulus; (B) intravenous injection of PEAK-DMA, EPR effect-mediated tumor accumulation, and tumor extracellular acidity-triggered sphere-to-rod shape switch; (C) improved internalization of rod-like nanoparticles in tumor cells and enhanced PDT efficacy *in vivo*.

RESULTS AND DISCUSSION

Synthesis and Characterization of PEAK-DMA. Chimeric peptide PEAK was prepared through standard Fmoc solid phase peptide synthesis (SPPS) method. And electrospray ionization mass spectrometry (ESI-MS) confirmed the validity of PEAK (Figure S1). Multicharged peaks at 591.12 ([M+4Na]$^{4+}$) and 758.44 ([M+3H]$^{3+}$) were observed. Meanwhile, high-performance liquid chromatography (HPLC) spectrum indicated that the purity of PEAK was above 90% (Figure S2). Subsequently, PEAK was stirred with DMA at an alkaline environment to obtain PEAK-DMA. The sharp Soret band around 400 nm of PEAK-DMA in UV−vis spectrum indicated the decreased $\pi-\pi$ stacking among PpIX molecules (Figure 2A), when compared with free PpIX with broadened bands at 352 and 450 nm.[34,35] Decreased $\pi-\pi$ stacking facilitated the generation efficacy of reactive oxygen species (ROS) in PEAK-DMA. And 2′,7′-dichlorodihydrofluorescein diacetate (DCFH-DA) was used to monitor the generation of ROS, since nonfluorescence DCFH-DA could be rapidly oxidized into fluorescence dichlorofluorescein (DCF) in the presence of ROS. As shown in Figure 2B, the increase rate of fluorescence intensity in PEAK-DMA group was significantly higher than that in PpIX group with prolonging of irradiation time, suggesting the improved ROS generation efficacy of PEAK-DMA.

Mild Acidity-Triggered DMA Detachment and Geometrical Shape Switch of PEAK-DMA. It was recognized that dimethylmaleic amide could undergo rapid hydrolysis under mildly acidic environment via intramolecular catalysis assisted by nearby carboxylic acid group. Therefore, PEAK-DMA was expected to detach DMA groups and expose primary amine at mildly acidic environment. Fluorescamine was employed as a sensor to monitor this process due to the fact that nonfluorescence fluorescamine would rapidly react with primary amine and emit green fluorescence. As shown in Figure 2C, fluorescence increment at pH 6.8 was significantly greater than that at pH 7.4 for PEAK-DMA. Apparently, acidic environment accelerated hydrolysis of PEAK-DMA, leading to rapid exposure of primary amine in Lys. For comparison, the fluorescence spectrum of fluorescamine in acidity-insensitive, succinic anhydride modified PEAK (designated as PEAK-SA) was recorded as a negative control. Negligible fluorescence increment was observed at both pHs of 6.8 and 7.4 when PEAK-SA was incubated with fluorescamine (Figure 2C). Unlike the dimethylmaleic amide in PEAK-DMA, the conformation of succinic amide was flexible in PEAK-SA. The terminal carboxyl group was not maintained in close proximity to amide group, so the hydrolysis rate of succinic amide was much slower than dimethylmaleic amide at acidic environment,[36] leading to dramatically retarded exposure of amino groups in PEAK-SA.

After amino groups got exposed, the subsequent protonation of Lys at acidic environment would change the surface potential. Here, dynamic zeta potentials of PEAK-DMA nanoparticles at pHs of 6.8 and 7.4 were recorded as a function of incubation time. It was found that PEAK-DMA was very

DOI: 10.1021/acsnano.7b00216
ACS Nano XXXX, XXX, XXX−XXX

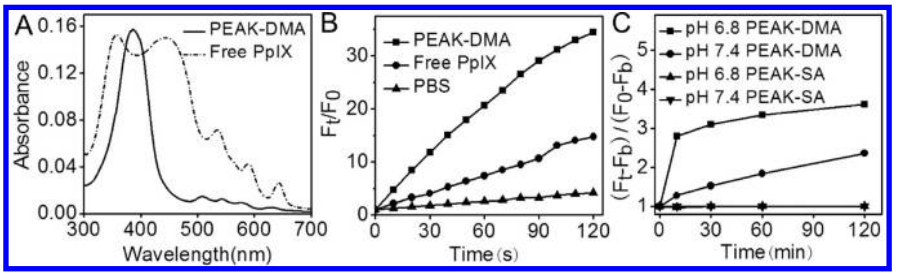

Figure 2. (A) UV−vis spectrum of PEAK-DMA and PpIX. (B) ROS generation of PEAK-DMA under different light irradiation times. (C) Detachment of DMA group in PEAK-DMA at pH 6.8 and 7.4. PEAK-SA was used as a control. Fluorescamine was used as the sensor.

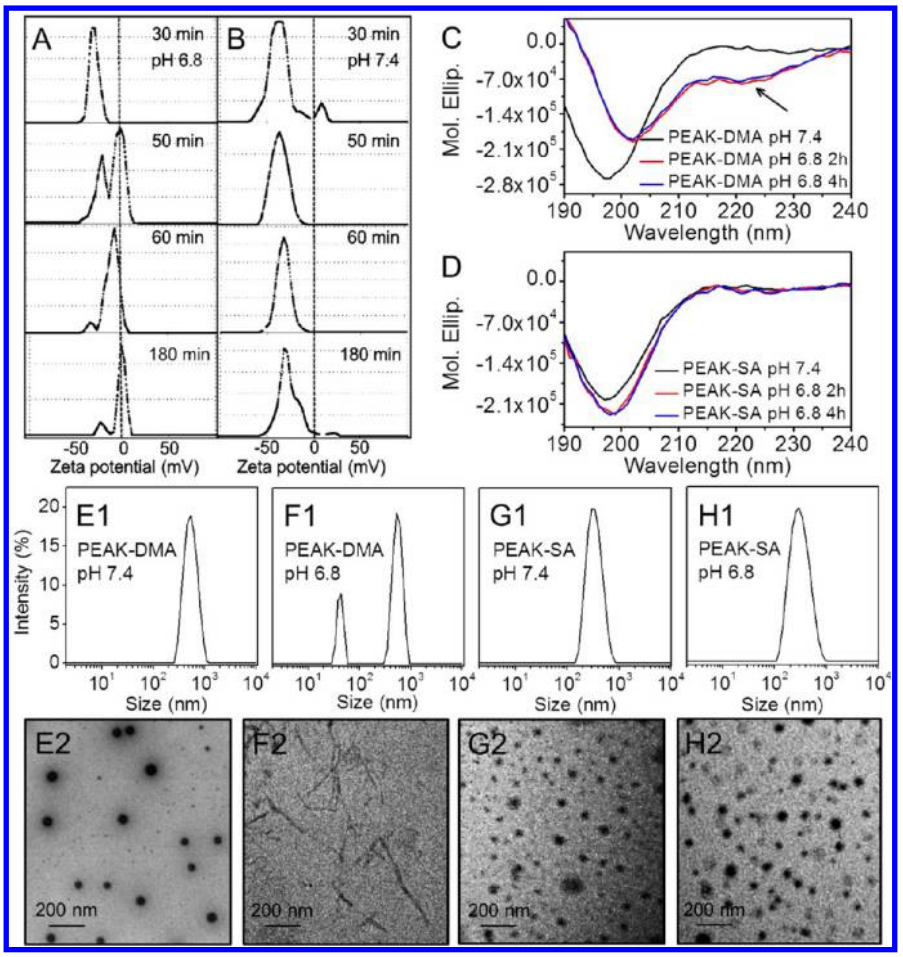

Figure 3. Zeta potential changes of PEAK-DMA as a function of time at (A) pH 6.8 and (B) pH 7.4. (C) CD spectrum of PEAK-DMA incubated at pH 6.8 for 2 and 4 h; (D) CD spectrum of PEAK-SA incubated at pH 6.8 for 2 and 4 h. PEAK-DMA and PEAK-SA incubated at pH 7.4 were used as controls, respectively. Hydrodynamic size and TEM images of PEAK-DMA at (E1, E2) pH 7.4 and (F1, F2) pH 6.8. Hydrodynamic size and TEM images of PEAK-SA at (G1, G2) pH 7.4 and (H1, H2) pH 6.8.

negatively charged at both pHs of 6.8 and 7.4 at 30 min due to the existence of abundant carboxylic acid groups in PEAK-DMA (Figure 3A and B). With prolonging of incubation time, zeta potential of PEAK-DMA at pH 7.4 changed little (Figure 3B). It only slightly increased from around −38 mV to −30 mV even at 180 min, suggesting that PEAK-DMA was relatively stable at pH 7.4. In sharp contrast, the peak of zeta potential at pH 6.8 moved right and split into two peaks of −20 mV and 0 mV at 50 min (Figure 3A), suggesting the detachment of DMA groups as well as increase of zeta potential at acidic environment. When the incubation time at pH 6.8 was further prolonged, the peak area around 0 mV gradually increased. At 180 min, the peak was close to 0 mV. Obviously, mild acidity-triggered detachment of DMA groups was time-dependent. As a control, PEAK-SA exhibited negligible change in zeta potential at both acidic and neutral environments (Figure S3). Zeta potentials were very negatively charged all the time (around −31 mV) due to the stability of succinic amide, when compared with dimethylmaleic amide.

Having evaluated the acidic responsiveness of PEAK-DMA, we proceeded to investigate the potential effect of DMA detachment on secondary structure of chimeric peptide via circular dichroism (CD) spectrum. As shown in Figure 3C and D, when PEAK-DMA and PEAK-SA were incubated at pH 7.4 (in PBS buffer), they exhibited strong negative peak at around 197 nm, suggesting that random coil structure existed in their

DOI: 10.1021/acsnano.7b00216
ACS Nano XXXX, XXX, XXX−XXX

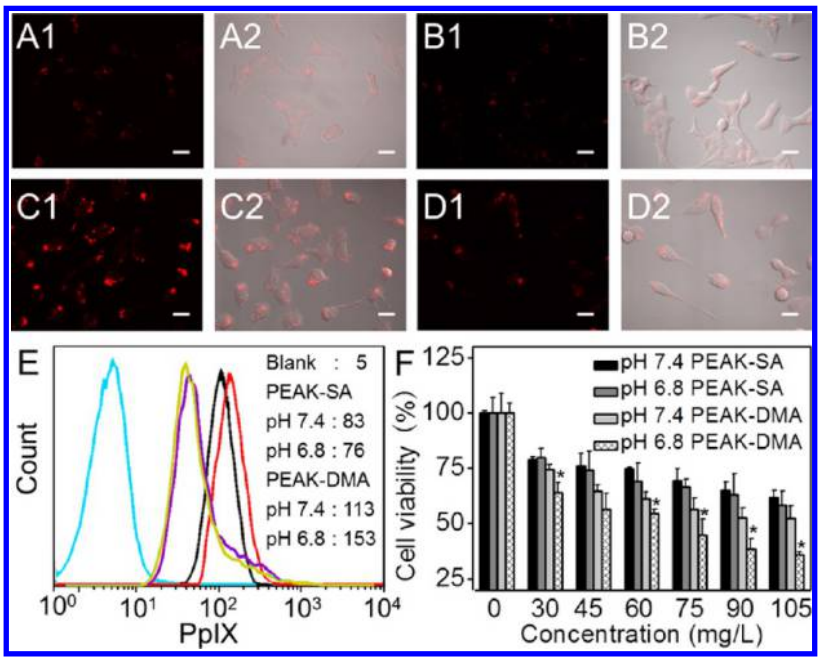

Figure 4. CLSM images of the cellular internalization in HeLa cells of PEAK-SA at (A1, A2) pH 6.8 and (B1, B2) pH 7.4; PEAK-DMA at (C1, C2) pH 6.8 and (D1, D2) pH 7.4. A2-D2: merged field. The scale bar was 20 μm. (E) Flow cytometry analysis and the corresponding MFI value of the cellular internalization of PEAK-SA and PEAK-DMA. Blue line: blank control; yellow line: PEAK-SA at pH 6.8; purple line: PEAK-SA at pH 7.4; black line: PEAK-DMA at pH 7.4; red line: PEAK-DMA at pH 6.8. (F) *In vitro* cytotoxicity of HeLa cells of PEAK-DMA and PEAK-SA at different pHs against HeLa cells with 50 s irradiation. *$p < 0.05$ was determined via a Student's t test, when the toxicity of PEAK-DMA at pH 6.8 was compared with that at pH 7.4.

molecular conformation due to strong electrostatic repulsion among carboxyl groups. Meanwhile, secondary structure of PEAK-SA did not change at pH 6.8 even for 4 h (Figure 3D). In contrast, secondary structure of PEAK-DMA dramatically changed at pH 6.8. The peak at 197 nm shifted to 202 nm while a new peak at around 222 nm appeared (Figure 3C), indicating the emergence of α-helix and β-strand conformations due to the detachment of DMA groups. This results were consistent with previous report.[37] The transition of secondary structure of PEAK-DMA at acidic environment would change the self-assemble behavior. To confirm it, dynamic light scattering (DLS) analysis of PEAK-DMA at pHs of 6.8 and 7.4 was conducted. As shown in Figure 3E1, only one peak around 535.7 nm was observed at pH 7.4, suggesting the formation of uniform assembly. However, two peaks (around 520.8 and 43.7 nm) were found at pH 6.8 (Figure 3F1), indicating that nonspherical assembly might generate at acidic environment. Meanwhile, DLS results revealed that PEAK-DMA at pH 6.8 was stable in the presence of serum proteins, especially when the incubation time was prolonged from 3 to 6 h (Figure S4). For comparison, hydrodynamic size of PEAK-SA did not change when pH decreased from 7.4 to 6.8 (Figure 3G1 and H1).

In order to get insight of the self-assembly behavior, transmission electron microscope (TEM) image was further conducted. As expected, substantially geometrical shape discrepancy of PEAK-DMA was observed. Well-dispersed and uniform spherical nanoparticles formed at pH 7.4 (Figure 3E2). And when PEAK-DMA was incubated at pH 6.8 for just 1.5 h, a great of rod nanoparticles had appeared (Figure S5A), which suggested the rapid shape switch of PEAK-DMA at pH 6.8. When PEAK-DMA was incubated at pH 6.8 for 3 h, it completely assembled into short rod-like nanoparticles (Figure 3F2), whose aspect ratio was mainly below 7 (Figure S5B and C). On the contrary, PEAK-SA always exhibited spherical nanoparticles regardless of pH decrease (Figure 3G2 and H2). Obviously, the results of TEM were consistent with that of DLS.[38] This sphere-to-rod geometrical shape switch of PEAK-DMA was due to the following facts: modification of DMA groups strongly shielded the positive charge amines in Lys residues and ionic complementarity between Lys and Glu in PEAK. In other words, electrostatic repulsion dominated the self-assemble behavior of PEAK-DMA. So amphiphilic random coil PEAK-DMA with typical core−shell structure could form spherical nanoparticles. However, at mildly acidic environment, DMA groups were detached. Positively charged Lys and negatively charged Glu were distributed alternatively. As a result, the electrostatic interaction was recovered and hydrophobic interaction among Ala residues was enhanced, which led to the formation of α-helix and β-strand conformations and drove the formation of short rod-like assembly.

Furthermore, the critical association number (CAC) of PPEAK-DMA at pHs of 6.8 and 7.4 was determined via fluorescence technique using pyrene as a hydrophobic probe. It was found that CAC for the spheres (pH 7.4) and the rods (pH 6.8) were 11.4 and 7.5 mg/L, respectively (Figure S6A and B). These small CAC values indicated the potential application of PEAK-DMA in a diluted medium, such as body fluids. It was also noted that CAC value at pH 6.8 was smaller than that at pH 7.4, suggesting that the recovered electrostatic interaction could drive the formation of assembly at lower concentration. The morphology of PEAK-DMA at pHs of 6.8 and 7.4 with a low concentration (12 mg/L) was also observed. Spherical nanoparticles were still observed at pH 7.4 (Figure S6C) and rod nanoparticles were found at pH 6.8 (Figure S6D), suggesting that decreasing the concentration of PEAK-DMA would not affect the self-assembly dramatically.

DOI: 10.1021/acsnano.7b00216
ACS Nano XXXX, XXX, XXX−XXX

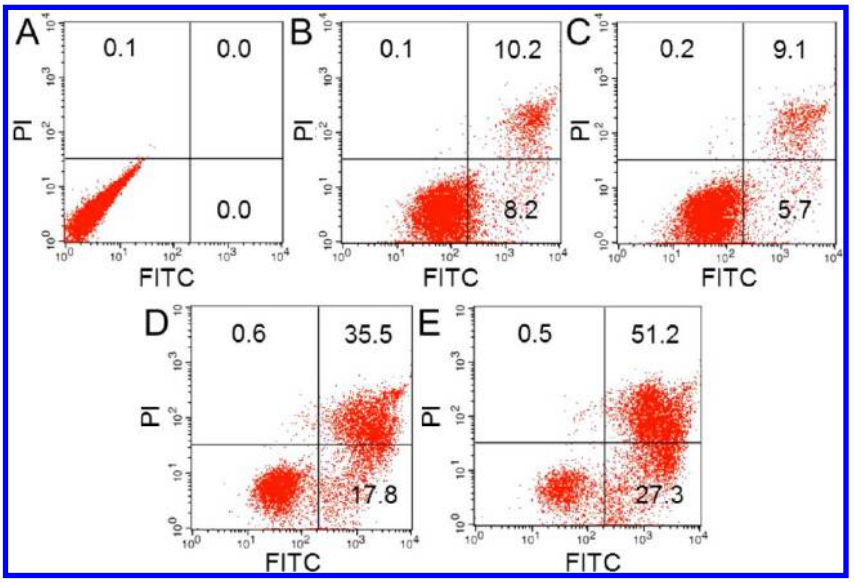

Figure 5. Cell apoptotic analysis via Annexin V-FITC/PI assay: (A) blank control; (B) PEAK-SA at pH 7.4; (C) PEAK-SA at pH 6.8; (D) PEAK-DMA at pH 7.4; (E) PEAK-DMA at pH 6.8.

Tumor Extracellular Acidity-Triggered Enhanced Cellular Internalization of PEAK-DMA. In light of the fact that different from normal tissue whose pH was 7.3−7.4, tumor tissue was mildly acidic (pH 6.3−6.9).[39] Meanwhile, geometrical shape would affect the cellular internalization of nanoparticles. Therefore, PEAK-DMA was expected to show a relative selectivity between tumor cells and normal cells. Cellular internalization behavior of PEAK-DMA was observed via confocal laser scanning microscopy (CLSM) and PEAK-SA was used as a control. Human cervical carcinoma (HeLa) cells were incubated with samples at pHs of 6.8 and 7.4 to simulate tumor acidic extracellular environment and neutral physiological environment (normal tissue), respectively. For PEAK-SA, a not obvious difference in red fluorescence was observed at pHs of 6.8 (Figure 4A1) and 7.4 (Figure 4B1), and the red fluorescence was weak due to the electrostatic repulsion between PEAK-SA and negatively charged cell membranes at these pHs. In contrast, for PEAK-DMA, remarkably stronger intensity and larger area of red fluorescence was observed at pH 6.8 (Figure 4C1), when compared with that at pH 7.4 (Figure 4D1). Considering that the fluorescence at pH 6.8 was slightly lower than that at pH 7.4 for PEAK-DMA according to fluorescence spectrum (Figure S7), these results indicated the improved cellular internalization of PEAK-DMA at pH 6.8. Amplified images of merged field were also performed in Figure S8. Meanwhile, internalization of PEAK-DMA was time-dependent (Figure S9). Clearly, this sphere-to-rod shape switch accelerated cellular internalization and endowed PEAK-DMA with tumor selectivity. It was known that different from spherical nanoparticles that theoretically had just one contact point with cell membranes, rod-like nanoparticles have multivalent interaction with cell membranes.[24] Meanwhile, the hydrophobic blocks that could interact with cell membrane in rod-like particles were less shielded than that in spherical particles.[26] As a result, it exhibited stronger adhesion and more contact sites with cell membranes, achieving enhanced cellular internalization.[40] This shape-dependent difference in cellular internalization was consistent with previous reports.[24−26,41−43] The quantitative results of flow cytometry further confirmed this conclusion (Figure 4E). The mean fluorescence intensity (MFI) value of PEAK-DMA at pH 6.8 was 1.36-fold to that at pH 7.4, while MFI value of PEAK-SA at pH 6.8 was very close to that at pH 7.4. Meanwhile, MFI value of PEAK-DMA at pH 7.4 was higher than that of PEAK-SA at pH 6.8 or 7.4, since DMA groups in PEAK-DMA would be gradually liberated at pH 7.4, which would lead to geometrical shape switch to some extent inevitably.

Note that zeta potential of PEAK-DMA increased to some extent when pH decreased, it might potentially influence internalization process of nanoparticles. To confirm that shape switch but not increased zeta potential determined tumor accelerated internalization, DMA modified PpIX-Ahx-(Gly-Glu-Gly-Glu-Gly-Lys-Gly-Lys)$_2$ (denoted as PEGK-DMA) was employed as a negative control. ESI-MS of PEGK was performed in Figure S10A. PEGK-DMA also exhibited mildly acidic responsive increment of zeta potential due to the existence of DMA groups (Figure S10B). However, TEM images revealed that acidic environment would not trigger the sphere-to-rod shape switch (Figure S10C and D). Since Ala residues were replaced with Gly residues, β-sheet structure of chimeric peptide would be destroyed and the hydrophobic interaction among Ala residues also disappeared, which disfavored the formation of rod-like self-assembly.[31] Subsequently, PEGK-DMA was incubated with HeLa cells at pHs of 6.8 and 7.4, respectively. Negligible difference was found in cellular internalization between pH 6.8 and 7.4 (Figure S10E). And both the red signals at pHs of 6.8 and 7.4 were weak. Quantitative results in flow cytometry further confirmed it (Figure S10F). Apparently, although tumor acidic environment could increase zeta potential of PEGK-DMA to some extent, when compared with physiological environment, it would not improve the cellular internalization observably. It was probably due to the formation of zwitterionic-like compound of both PEAK-DMA and PEGK-DMA under acidic environment, which would not significantly accelerate cellular uptake, when compared with negatively charged biosubstances.[44,45]

Furthermore, tumor selective internalization of PEAK-DMA was verified by cell viability. Samples were incubated with HeLa cells for 4 h at pH 6.8 or 7.4 and the medium was replaced. Subsequently, cells received 50 s light irradiation. Cells viability

DOI: 10.1021/acsnano.7b00216
ACS Nano XXXX, XXX, XXX−XXX

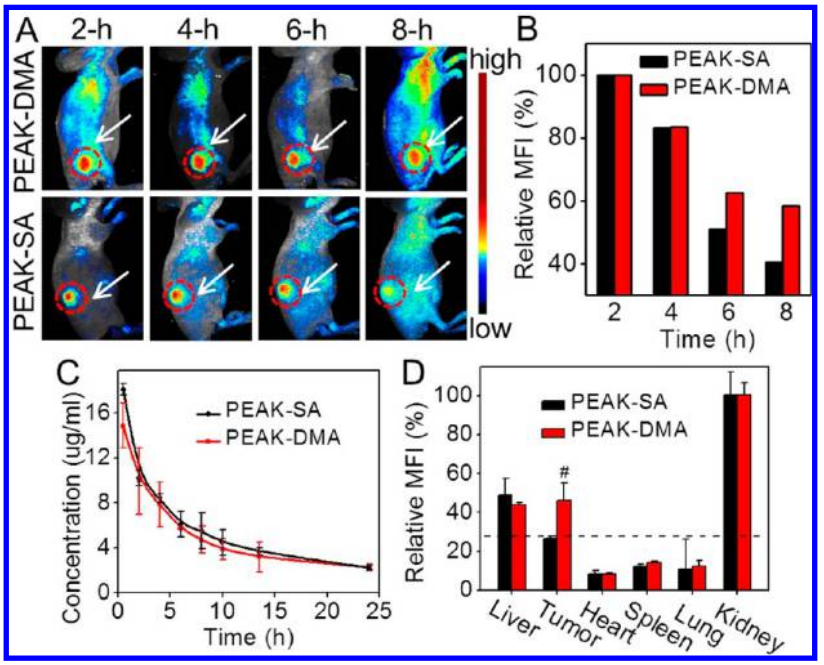

Figure 6. (A) *In vivo* fluorescence images of H22 tumor-bearing mice at preset time after intravenous injection. Note that PEAK-DMA in deep organs, such as liver and spleen, were not detected due to the limited penetration depth of visible light. (B) Relative MFI value of PpIX in tumor region and the average fluorescence signal at the 2 h was set as 100%. (C) Pharmacokinetics of PEAK-DMA and PEAK-SA (PpIX: 3 mg/kg body weight) after intravenous injection. Three mice were used for each group. (D) Relative MFI values (relative to kidney) of fluorescence signals of tumor and normal organs.

was determined via MTT assay. As shown in Figure 4F, PEAK-SA exhibited similar cytotoxicity at both pHs of 6.8 and 7.4. And cytotoxicity of PEAK-DMA at pH 6.8 was significantly higher than that at pH 7.4 due to the geometrical shape switch-mediated enhanced cellular uptake as proved above. Besides, PEAK-DMA performed higher cytotoxicity than PEAK-SA at same condition, since PEAK-DMA performed elevated cellular internalization, when compared with PEAK-SA. All these results were consistent with that of quantitatively cellular internalization. Note that the cytotoxicity difference between pH 6.8 and 7.4 became greater when the concentration of PEAK-DMA increased. This was probably due to the fact that PEAK-DMA with higher concentration would prefer to reassemble. More spherical nanoparticles would switch to rod shape when the concentration of PEAK-DMA was higher. As a result, more rod nanoparticles at pH 6.8 could be internalized by cells, when compared with spherical nanoparticles at pH 7.4.[46,47]

Subsequently, Annexin V-FITC/propodium iodide (PI) assay was conducted. As shown in Figure 5, PEAK-DMA could initiate certain cell apoptosis during PDT. More important, the cell death proportion mediated by PEAK-DMA at pH 6.8 during PDT was higher than that at pH 7.4. For comparison, negligible difference was observed for PEAK-SA in inducing cell death between pH 6.8 and 7.4. These results of cell apoptosis were consistent with that of CLSM and cytotoxicity, which further confirmed the tumor selective internalization of PEAK-DMA.

Tumor Targeted Imaging and Pharmacokinetics *in Vivo*. To demonstrate the feasibility of PEAK-DMA for tumor targeting *in vivo*, the biodistribution imaging *in vivo* at different time points was recorded. H22 tumor-bearing nude mouse was chosen as the animal model. PEAK-SA was used as a control. As shown in Figure 6A, both PEAK-DMA and PEAK-SA could accumulate quickly in tumor tissue at the 2 h due to enhanced permeability and retention (EPR) effect. With prolonging of incubation time, fluorescence in PEAK-SA group rapidly decreased especially at the 8 h. This was attributed to the metabolism *in vivo*. In sharp contrast, the fluorescence in PEAK-DMA group decreased slowly. Obvious fluorescence was observed at the 8 h. The quantitatively relative MFI value of PpIX in tumor region further confirmed it (Figure 6B). The relative MFI values of PEAK-DMA and PEAK-SA in tumor region decreased to 59% and 41% at the 8 h, respectively. Clearly, sphere-to-rod shape switch enhanced internalization of chimeric peptide in tumor cells, which avoided metabolic clearance and prolonged the retention in tumor. In addition, the rod shape of PEAK-DMA at pH 6.8 in the presence of 1% serum was confirmed via TEM (Figure S11A), while the spherical shape of PEAK-DMA in neutral blood was exhibited in Figure S12. Herein, 10% serum was not used since the high concentration of serum would lead to formation of thick layer under vacuum state (Figure S11B), which significantly affected the morphology observation.

It was documented that longer blood circulation of nanoparticles in blood-stream could provide a greater opportunity to accumulate in tumor tissues through EPR effect. To verify that the prolonged retention in tumor region of PEAK-DMA relied on tumor-triggered sphere-to-rod shape switch, but not the discrepancy in blood circulation time, pharmacokinetic study of PEAK-DMA and PEAK-SA was performed.[48,49] As shown in Figure 6C, both PEAK-DMA and PEAK-SA exhibited a relative long circulation time. Meanwhile, the concentration of PEAK-DMA at 3 h post *in vivo* injection was remarkably higher than the CAC value (7.5 mg/L) of rod at acidic environment, which ensured the geometric shape switch of PEAK-DMA in tumor. This long circulation time was attributed to the negatively or neutrally charged surface of

DOI: 10.1021/acsnano.7b00216
ACS Nano XXXX, XXX, XXX−XXX

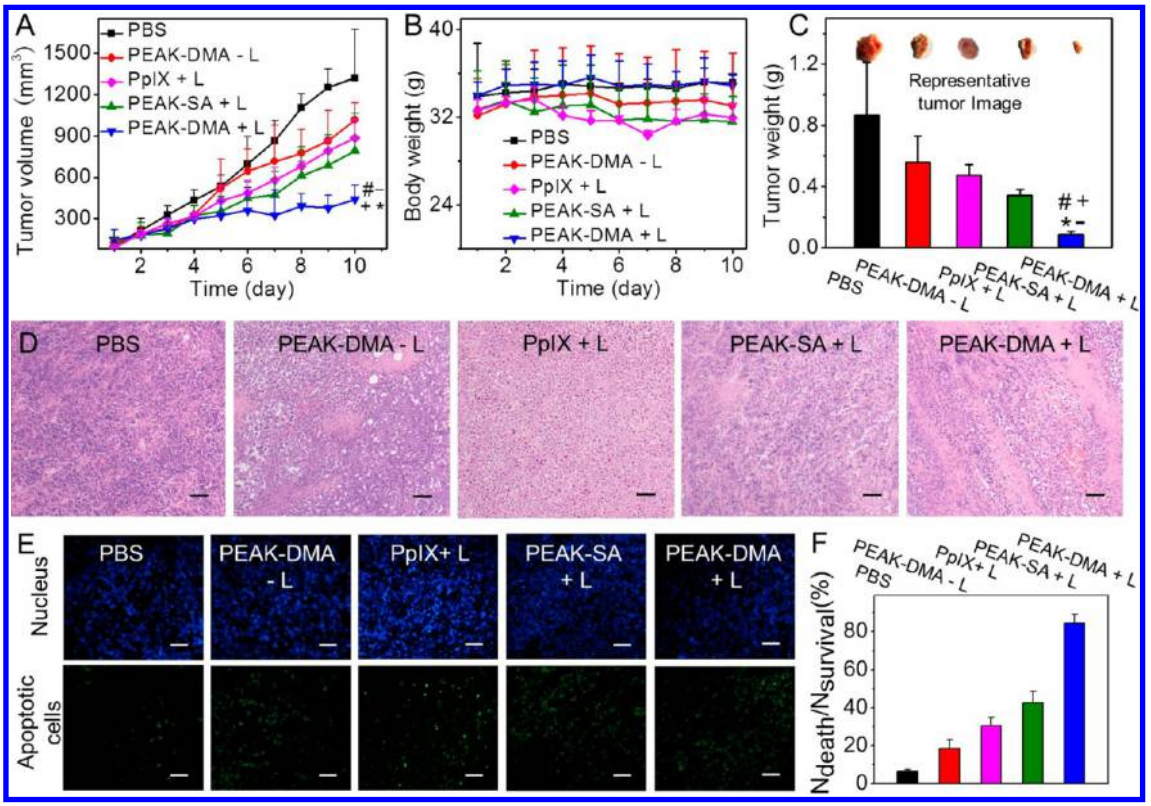

Figure 7. *In vivo* **antitumor efficacy and every group had four mice: (A) average tumor volume and (B) body weight with different treatments (PpIX: 4 mg/kg body weight). (C) Average tumor weight after 10 days treatment. Insert was the representative tumor image of various groups. (D) Histological observation of tumor tissues via H&E staining. (E) Detection of PDT-induced apoptosis in tumor tissues with TUNEL staining assay. Blue signal: cell nucleus; green signal: apoptotic cells. The scale bar was 50 μm. (F) Quantitatively statistical result of cell apoptosis under various treatments. "L" represented light irradiation. Injection of free PpIX in DMSO employed intraperitoneal injection but not i.v. injection, since i.v. injection of free PpIX would lead to the death of mice due to blockages.**

nanoparticles, which could resist protein adsorption in blood and retard metabolic clearance. In particular, similar pharmacokinetic behaviors were observed in PEAK-DMA and PEAK-SA groups, which substantially demonstrated that more efficient retention of PEAK-DMA in tumor was due to the geometric shape switch-mediated enhanced cellular internalization.

Subsequently, relative MFI of various organs and tumor tissue at the 24 h was calculated. Kidney was chosen as an internal reference. Figure 6D revealed that the relative MFI value in tumor of PEAK-DMA was significantly higher than that of PEAK-SA, which was agreement with the result of tumor imaging *in vivo*. Encouragingly, the accumulation of PEAK-DMA in tumor was slightly higher than that in primary metabolic organ liver, suggesting the well tumor target efficacy of PEAK-DMA *in vivo*. The enhanced accumulation of PEAK-DMA in tumor was also confirmed via CLSM of tumor tissue. As shown in Figure S13, the red signal of PEAK-DMA group in tumor was stronger than that of PEAK-SA group.

***In Vivo* Antitumor Study.** To confirm that enhanced tumor accumulation of PEAK-DMA can elevate PDT efficacy *in vivo*, H22 tumor-bearing mice were intravenously injected with various samples. As shown in Figure 7A, PBS and PEAK-DMA without light irradiation could not inhibit tumor growth. PpIX (intraperitoneal injection) and PEAK-SA with light irradiation could retard tumor growth to some extent, and PEAK-DMA with light irradiation exhibited most significant inhibition. Meanwhile, a modest change of body weight in PEAK-DMA group indicated that PAPP-DMA had negligible systemic toxicity during PDT (Figure 7B). When the treatment finished, tumor tissues were collected and weighed, representative tumor tissues were imaged (Figure 7C). As expected, significant difference was observed between PEAK-DMA and other groups in tumor image and weight, whose trend was similar to that of average tumor volume. Apparently, PEAK-DMA could realize enhanced PDT efficacy *in vivo* due to tumor acidity-triggered sphere-to-rod shape switch, accelerated cellular internalization, and prolonged tumor retention as proved above.

Furthermore, hematoxylin and eosin (H&E) staining was conducted to evaluate therapeutic efficacy. As shown in Figure 7D, tumor cells in both PBS group and PEAK-DMA group without light irradiation were dense. On the contrary, tumor cells in PEAK-DMA group with light irradiation presented greatest nuclei absence, suggesting that most tumor cells were dead in PEAK-DMA group during PDT.[50] In order to get direct insight of the potential therapeutic mechanism, terminal-deoxynucleoitidyl transferase mediated nick end labeling (TUNEL) assay was evaluated. As shown in Figure 7E, the green/blue fluorescence spot ratio observably increased in tumor tissue in the following order: PBS < PEAK-DMA without light irradiation < PpIX with light irradiation < PEAK-SA with light irradiation < PEAK-DMA with light irradiation. Quantitatively statistical result was also performed in Figure 7F. Obviously, PEAK-DMA exhibited most efficient PDT *in vivo*. Then PDT initiated cell apoptosis, resulting in the ablation of tumor.[51]

Systemic Toxicity Evaluation *in Vivo*. In order to assess the potential systemic toxicity of PEAK-DMA under light irradiation, blood routine analysis was performed to assess the

DOI: 10.1021/acsnano.7b00216
ACS Nano XXXX, XXX, XXX−XXX

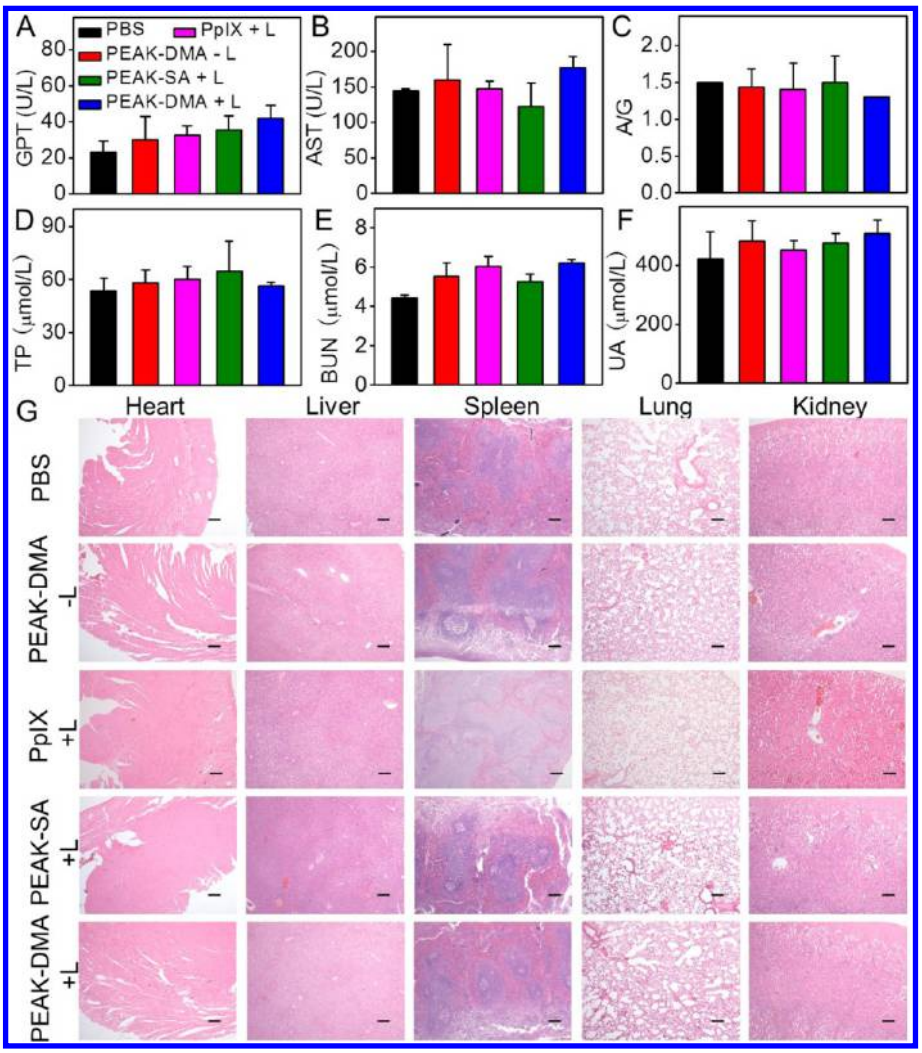

Figure 8. Blood routine analysis of various groups (three mice per group) after 10 days treatment: (A) GPT; (B) AST; (C) A/G; (D) TP; (E) BUN; and (F) UA. PpIX via intraperitoneal injection was used as a control. (G) Systemic toxicity evaluation via H&E staining of heart, liver, spleen, lung, and kidneys with different samples. "L" represented light irradiation. The scale bar was 100 μm.

potential liver and kidneys damage (Figure 8). Negligible difference was found among various groups in the expression level of liver function markers in terms of glutamic pyruvate transaminase (GPT, Figure 8A), aspartate aminotransferase (AST, Figure 8B), albumin/globulin ratio (A/G, Figure 8C), total serum protein (TP, Figure 8D), kidney function markers in terms of blood urea nitrogen (BUN, Figure 8E), and uricacid (UA, Figure 8F). These indexes were consistence with previous reports,[13,52] suggesting that no liver and kidney dysfunction was induced by PEAK-DMA during PDT, even PEAK-DMA appeared in liver or kidney inevitably during circulation. This negligible side effect was attributed to the fact that PEAK-DMA could efficiently accumulate in tumor region, and ROS had a very limited action distance and short half-life period, which efficiently restricted phototoxicity in tumor region. In addition, physiological morphology of various organs was observed via H&E staining to visually evaluate the side effects. Figure 8G showed that the physiological morphologies of spleen, lung, heart, liver, and kidneys of various groups were normal, no pathological changes were observed. Taken together, PEAK-DMA with tumor acidity-triggered geometrical shape switch achieved enhanced PDT and minimal side effects *in vivo*.

CONCLUSIONS

In summary, we designed an amphiphilic chimeric peptide, PEAK-DMA, to realize mild acidity-triggered geometrical shape switch and enhanced tumor internalization. PEAK-DMA could self-assemble into spherical nanoparticles with well EPR effect. Once arriving at tumor region during circulation, PEAK-DMA underwent acidity-responsive detachment of DMA groups and geometrical shape switch. The resulting rod-like nanoparticles in tumor microenvironment promoted cellular internalization of chimeric peptide, which further prolonged the retention time in tumor and enhanced PDT efficacy with negligible side effects. This drug delivery system demonstrated here with tumor microenvironment responsive shape switch should show great potential in targeted tumor therapy.

MATERIALS AND METHODS

Materials. 2-Chlorotrityl chloride resin, *N*-fluorenyl-9-methoxycarbonyl (Fmoc)-protected L-amino acids, diisopropylethylamine (DiEA), *o*-benzotriazole-*N*,*N*,*N*′,*N*′-tetramethyluroniumhexafluorophosphate (HBTU) and piperidine were purchased from GL Biochem Ltd. (Shanghai, China). Dulbecco's modified Eagle's medium (DMEM), trypsin, fetal bovine serum (FBS), MTT, penicillin-streptomycin were purchased from GIBCO Invitrogen Corp.

DOI: 10.1021/acsnano.7b00216
ACS Nano XXXX, XXX, XXX−XXX

Triisopropylsilane (TIS) and trifluoroacetic acid (TFA) were obtained from Shanghai Reagent Chemical Co. (China). Fluorescamine, succinic anhydride, Fmoc-Ahx-COOH, and DMA were provided by Sigma-Aldrich (USA). All other reagents were used without further purification.

Synthesis of PEAK. PEAK or PEGK was manually prepared via a SPPS method on 2-chlorotrityl chloride resin. HBTU/DiEA was used to catalyze the reaction. 20% piperidine/DMF (v/v) was used to remove Fmoc group. Product was cleaved from the resin by adding the mixture of TFA, TIS, and H_2O in the volume ratio of 95:2.5:2.5 for 1.5 h. Then chimeric peptide was precipitated in cold anhydrous diethyl ether. The crude product was separated from the solvent by centrifugation, followed by drying under vacuum overnight. Chimeric peptide was dissolved in distilled water for freeze-drying. Chimeric peptide was purified via HPLC with a C18 column by a gradient elution with the mobile phase of A: 0.1% TFA in 100% acetonitrile and B: 0.1% TFA in 100% water. The gradient was: 0−0.01 min 17% A and 83% B; 0.01−20 min 67% A and 33% B; 25−25.01 min 100% mobile phase A. The molecular weight was tested by ESI-MS.

Synthesis of PEAK-DMA. PEAK (10 mg) and 3.5 equiv (to amino group) of DMA (7.8 mg) were dissolved in DI water. NaOH (0.2 mol/L) was added dropwise to keep pH around 10. After 24 h reaction in dark, the solution was subjected to dialysis (MWCO 500 Da) against water at pH 10 for 6 h. Water was replaced every 1.5 h. Then PEAK-DMA was obtained via freeze-drying. As controls, PEGK-DMA, and PEAK-SA were obtained via the similar method.[53]

Characterization of PAPP-DMA. UV−vis spectrum of PEAK-DMA (30 mg/L) was determined at pH 10 (in NaOH solution).[54] Morphology of PEAK-DMA nanoparticles (105 mg/L) at pHs of 6.8 and 7.4 was observed by TEM (JEM-2100 microscope). The hydrodynamic size and zeta potential of PEAK-DMA were measured by Nano-ZS ZEN3600 (Malvern Instruments) at 25 °C in PBS buffer. PEAK-SA and PEGK-DMA were used as controls.

Degradation of DMA in PEAK-DMA. Degradation of DMA was measured by the fluorescamine method. Briefly, PEAK-DMA (50 mg/L) was incubated at pH 6.8 or 7.4 with specified times of 0, 10, 30, 60, and 120 min. Then all samples were mixed with fluorescamine solution (2 mg/mL in DMF, 2 mL) for 10 min at room temperature. Afterward, fluorescence intensity at preset time (F_t) was determined by fluorospectrophotometer (excitation wavelength (Ex): 365 nm, emission wavelength (Em): 475 nm). Fluorescence intensity of PBS was set as F_b. Fluorescence intensity of sample at 0 min was set as F_0. The degradation of DMA was calculated as following: $(F_t - F_b)/(F_0 - F_b) \times 100\%$.

ROS Detection. The generation of ROS was measured via fluorescence spectrum using DCFH-DA as the sensor. PEAK-DMA (50 μL, 1 mg/mL) was mixed with 30 μL DCFH-DA (1 mg/mL) and 920 μL water. The fluorescence intensity were recorded (Ex: 485 nm) at preset times with 630 nm light irradiation. PpIX in 0.05% DMSO was used as a negative control. The ROS generation ability was calculated as F_t/F_0. The initial fluorescence of NaOH pretreated DCFH-DA alone was defined as F_0.

CD Spectrum. PEAK-DMA or PEAK-SA was incubated at pH 6.8 for 2 and 4 h and then the secondary structure was recorded on a J-1500 spectropolarimeter (Jasco, Japan). Quartz cell was used throughout. The spectra were scanned from 240 to 190 nm for three times. PEAK-DMA and PEAK-SA at pH 7.4 were used as controls.

CAC Determination. The CAC values of PEAK-DMA at pHs of 6.8 and 7.4 were determined via fluorescence spectroscopy. Pyrene was used as the hydrophobic fluorescent probe. Various concentrations of PEAK-DMA solutions (0−0.1 mg/mL, pHs of 6.8 and 7.4) with 6×10^{-7} M pyrene were prepared, respectively. Emission wavelength was chosen at 390 nm while excitation spectra ranging from 300 to 360 nm were recorded. Excitation and emission bandwidths were 10 nm. Fluorescence spectra were recorded and the change of the intensity ratio of the third and first vibronic bands (I_3/I_1) was plotted against the logarithm of peptide concentrations. CAC was determined based on the crossover point at low concentration on this plot.

Cellular Uptake Evaluation *in Vitro*. Cellular uptake was investigated via both CLSM and flow cytometry. For CLSM observation, HeLa cells were seeded in 6-well plates and incubated in DMEM supplemented with 10% FBS for 24 h. Thereafter, the medium was removed and PEAK-DMA (105 mg/L) in fresh medium (pH 6.8 or 7.4) were added. The culture medium was removed, followed by repeated wash with PBS at 4 h post incubation. Subsequently, samples were imaged via CLSM. For flow cytometry analysis, cells were treated in a similar way. After internalization for 4 h, cells were treated with trypsin and then collected. Cells were washed and resuspended in PBS. Samples were detected via a FACS Calibur flow cytometer (BD Biosciences, USA). The results were analyzed with Flow-jo software.

Cytotoxicity Assay *in Vitro*. The *in vitro* cytotoxicity of PEAK-DMA against HeLa cells were determined by MTT assay. Briefly, HeLa cell were seeded on 96-well plates at a density of 6000 cells/well and incubated for 24 h. Then medium was replaced with various concentrations of PEAK-DMA at pH 6.8 or 7.4, respectively. The culture medium was replaced with 200 μL of fresh medium (pH 7.4) at 4 h post incubation. Then cells received 50 s light irradiation (630 nm, 10 mW/cm^2) and then further incubated for 48 h. Afterward, MTT (5 mg/mL, 20 μL per well) was added. Four hours later, the supernatant was replaced with 150 μL of DMSO to dissolve the formazane. The optical density (OD) at 490 nm was determined via a microplate reader (Bio-Rad, Model 550, USA). The relative cell viability was calculated based on the formula: cell viability (%) = $OD_{(sample)}/OD_{(control)} \times 100\%$. $OD_{(sample)}$ was the OD value in the presence of sample and $OD_{(control)}$ was the optical density in the absence of sample.

Annexin V-FITC/PI Assay *in Vitro*. HeLa cells were seeded in 6-well plates and incubated in DMEM supplemented with 10% FBS for 24 h. Then the medium was removed and samples (105 mg/L) in fresh medium (pH 6.8 or 7.4) were added. The culture medium was removed, followed by repeated wash with PBS at 4 h post incubation. Subsequently, cells received 50 s light irradiation (630 nm, 10 mW/cm^2) and then further incubated for 12 h. Cells were collected and washed with PBS. Finally, cells were stained with Annexin V-FITC and propodium iodide (PI) for 10 min before detected via flow cytometry.

Optical Imaging, Tissue Distributions, and Pharmacokinetics *in Vivo*. Animal experiments were conducted in compliance with the criteria of The National Regulation of China. For optical imaging investigation, PEAK-DMA and PEAK-SA were intravenously injected into H22 tumor-bearing nude mice through tail vein. The equivalent PpIX dosages of each formulation were 3 mg/kg. Mice were anesthetized at the preset times and imaged directly via small animal imaging system in Institute of Virology (Wuhan, Chinese Academy of Sciences). For tissue distributions study, mice were sacrificed at 24 h post injection. The heart, liver, spleen, lung, kidney, and tumor were exfoliated and imaged. Furthermore, the tumor tissue was frozen section, and the fluorescence in tumor tissue was observed via CLSM. For pharmacokinetics study, blood samples of mice were obtained after intravenous injection for preset times. The blood samples were diluted with appropriate volume of PBS, followed by repeatedly freeze−thawed. Subsequently, cells were under ultrasound for 5 min, the fluorescence intensity of PpIX (Ex: 409 nm; Em: 630 nm) was recorded by fluorospectrophotometer.

Antitumor Effect *in Vivo*. 10^7 of H22 tumor cells were subcutaneous injected into the back of mice. When the volume of H22 tumor xenograft reached around 100 mm^3, mice were randomly divided into 5 groups. Mice were intravenously injected with PBS buffer, PEAK-DMA, and PEAK-SA (PpIX concentration: 4 mg/kg) every day, respectively. For PpIX group, PpIX in DMSO was intraperitoneally injected and the volume of DMSO was 50 μL. Six hours later, the two groups of PEAK-DMA received 0 min or 10 min light irradiation (638 nm) at a power density of 0.2 W/cm^2, respectively. As a control, PEAK-SA group and PpIX group also received 10 min light irradiation. The tumor volume and weight were measured every day before injection. The tumor volume was calculated as following: $a \times b^2/2$, a and b referred to the length and width of tumor, respectively.

DOI: 10.1021/acsnano.7b00216
ACS Nano XXXX, XXX, XXX−XXX

Systemic Toxicity *in Vivo*. For histological observation, mice were sacrificed at the 10th day. The organs and tumor were collected and fixed by 4% formalin, embedded in paraffin for H&E staining and TUNEL assay. For serum analysis, the mice blood was extracted from different mice groups at the 10th day. The blood samples were solidified and centrifuged at 3000 rpm for 5 min to obtain serum. Serum samples were detected at Union Hospital (Wuhan, China) and data were mean of three replicates.

Statistical Analysis. The statistical analysis was conducted by Student's *t* test. The differences were considered to be statistically significant for p value < 0.05.

ASSOCIATED CONTENT

Supporting Information

The Supporting Information is available free of charge on the ACS Publications website at DOI: 10.1021/acsnano.7b00216.

HPLC and ESI-MS of PEAK; zeta potential of PEAK-SA at pHs of 6.8 and 7.4; hydrodynamic size of PEAK-DMA in the presence of 10% serum protein; aspect ratio of PEAK-DMA self-assembly; amplified images of merged field of PEAK-SA and PEAK-DMA at pHs of 6.8 and 7.4; fluorescence spectrum of PEAK-DMA and PEAK-SA at pHs of 6.8 and 7.4; internalization of PEAK-DMA at pH 6.8 with time prolonging; characterizations of PEGK-DMA; TEM image of PEAK-DMA at pH 6.8 in the presence of serum; and CLSM images of tumor tissues (PDF)

AUTHOR INFORMATION

Corresponding Author

*E-mail: hyhan@mail.hzau.edu.cn.

ORCID

Xianzheng Zhang: 0000-0001-6242-6005

Heyou Han: 0000-0001-9406-0722

Notes

The authors declare no competing financial interest.

ACKNOWLEDGMENTS

This work was financially supported by National Natural Science Foundation of China (51603080 and 21375043) and the Fundamental Research Funds for the Central Universities (2662015QD026). We would like to thank the Center for Instrumental Analysis and Metrology, Institute of Virology, Chinese Academy of Science for our *in vivo* imaging work and we are grateful to Juan Min for her help in analyzing *in vivo* imaging data.

REFERENCES

(1) Mura, S.; Nicolas, J.; Couvreur, P. Stimuli-Responsive Nanocarriers for Drug Delivery. *Nat. Mater.* **2013**, *12*, 991−1003.

(2) Li, H. J.; Du, J. Z.; Du, X. J.; Xu, C. F.; Sun, C. Y.; Wang, H. X.; Cao, Z. T.; Yang, X. Z.; Zhu, Y. H.; Wang, J.; et al. Stimuli-Responsive Clustered Nanoparticles for Improved Tumor Penetration and Therapeutic Efficacy. *Proc. Natl. Acad. Sci. U. S. A.* **2016**, *113*, 4164−4169.

(3) Peer, D.; Karp, J. M.; Hong, S.; Farokhzad, O. C.; Margalit, R.; Langer, R. Nanocarriers as an Emerging Platform for Cancer Therapy. *Nat. Nanotechnol.* **2007**, *2*, 751−760.

(4) Cheng, L.; Wang, C.; Feng, L. Z.; Yang, K.; Liu, Z. Functional Nanomaterials for Phototherapies of Cancer. *Chem. Rev.* **2014**, *114*, 10869−10939.

(5) Marcucci, F.; Stassi, G.; De Maria, R. Epithelial-Mesenchymal Transition: a New Target in Anticancer Drug Discovery. *Nat. Rev. Drug Discovery* **2016**, *15*, 311−325.

(6) Park, D. H.; Cho, J.; Kwon, O. J.; Yun, C. O.; Choy, J. H. Biodegradable Inorganic Nanovector: Passive *versus* Active Tumor Targeting in siRNA Transportation. *Angew. Chem., Int. Ed.* **2016**, *55*, 4582−4586.

(7) Paris, J. L.; Cabañas, M. V.; Manzano, M.; Vallet-Regí, M. Polymer-Grafted Mesoporous Silica Nanoparticles as Ultrasound-Responsive Drug Carriers. *ACS Nano* **2015**, *9*, 11023−11033.

(8) Callmann, C. E.; Barback, C. V.; Thompson, M. P.; Hall, D. J.; Mattrey, R. F.; Gianneschi, N. C. Therapeutic Enzyme-Responsive Nanoparticles for Targeted Delivery and Accumulation in Tumors. *Adv. Mater.* **2015**, *27*, 4611−4615.

(9) Nazemi, A.; Boott, C. E.; Lunn, D. J.; Gwyther, J.; Hayward, D. W.; Richardson, R. M.; Winnik, M. A.; Manners, I. Monodisperse Cylindrical Micelles and Block Comicelles of Controlled Length in Aqueous Media. *J. Am. Chem. Soc.* **2016**, *138*, 4484−4493.

(10) Wei, H.; Zhuo, R. X.; Zhang, X. Z. Design and Development of Polymeric Micelles with Cleavable Links for Intracellular Drug Delivery. *Prog. Polym. Sci.* **2013**, *38*, 503−535.

(11) Chen, Q.; Feng, L. Z.; Liu, J. J.; Zhu, W. W.; Dong, Z. L.; Wu, Y. F.; Liu, Z. Intelligent Albumin-MnO_2 Nanoparticles as pH-/H_2O_2-Responsive Dissociable Nanocarriers to Modulate Tumor Hypoxia for Effective Combination Therapy. *Adv. Mater.* **2016**, *28*, 7129−7136.

(12) Tang, L.; Yang, X. J.; Yin, Q.; Cai, K. M.; Wang, H.; Chaudhury, I.; Yao, C.; Zhou, Q.; Kwon, M.; Cheng, J. J.; et al. Investigating The Optimal Size of Anticancer Nanomedicine. *Proc. Natl. Acad. Sci. U. S. A.* **2014**, *111*, 15344−15349.

(13) Han, K.; Wang, S. B.; Lei, Q.; Zhu, J. Y.; Zhang, X. Z. Ratiometric Biosensor for Aggregation-Induced Emission-Guided Precise Photodynamic Therapy. *ACS Nano* **2015**, *9*, 10268−10277.

(14) Ge, Z. S.; Liu, S. Y. Functional Block Copolymer Assemblies Responsive to Tumor and Intracellular Microenvironments for Site-Specific Drug Delivery and Enhanced Imaging Performance. *Chem. Soc. Rev.* **2013**, *42*, 7289−7325.

(15) Qiao, Z. Y.; Qiao, S. L.; Fan, G.; Fan, Y. S.; Chen, Y.; Wang, H. One-Pot Synthesis of pH-Sensitive Poly(RGD-co-*β*-amino ester)s for Targeted Intracellular Drug Delivery. *Polym. Chem.* **2014**, *5*, 844−853.

(16) Morachis, J. M.; Mahmoud, E. A.; Almutairi, A. Physical and Chemical Strategies for Therapeutic Delivery by Using Polymeric Nanoparticles. *Pharmacol. Rev.* **2012**, *64*, 505−519.

(17) Bhosale, S. V.; Nalage, S. V.; Booth, J. M.; Gupta, A.; Bhargava, S. K.; Bhosale, S. V. Solvent Induced Ordered-Supramolecular Assembly of Highly Branched Protoporphyrin IX Derivative. *Supramol. Chem.* **2012**, *24*, 779−788.

(18) Bhosale, S. V.; Bhosale, S. V.; Shitre, G. V.; Bobe, S. R.; Gupta, A. Supramolecular Chemistry of Protoporphyrin IX and Its Derivatives. *Eur. J. Org. Chem.* **2013**, *2013*, 3939−3954.

(19) Bhosale, S. V.; Kalyankar, M. B.; Nalage, S. V.; Bhosale, S. V.; Lalander, C. H.; Langford, S. J. Supramolecular Self-Assembled Nanowires by the Aggregation of a Protoporphyrin Derivative in Low-Polarity Solvents. *Supramol. Chem.* **2011**, *23*, 563−569.

(20) Geisbert, T. W.; Jahrling, P. B. Exotic Emerging Viral Diseases: Progress and Challenges. *Nat. Med.* **2004**, *10*, S110−S121.

(21) Barua, S.; Yoo, J. W.; Kolhar, P.; Wakankar, A.; Gokarn, Y. R.; Mitragotri, S. Particle Shape Enhances Specificity of Antibody-Displaying Nanoparticles. *Proc. Natl. Acad. Sci. U. S. A.* **2013**, *110*, 3270−3275.

(22) Geng, Y.; Dalhaimer, P.; Cai, S.; Tsai, R.; Tewari, M.; Minko, T.; Discher, D. E. Shape Effects of Filaments *versus* Spherical Particles in Flow and Drug Delivery. *Nat. Nanotechnol.* **2007**, *2*, 249−255.

(23) Herd, H.; Daum, N.; Jones, A. T.; Huwer, H.; Ghandehari, H.; Lehr, C. M. Nanoparticle Geometry and Surface Orientation Influence Mode of Cellular Uptake. *ACS Nano* **2013**, *7*, 1961−1973.

(24) Li, D.; Tang, Z. M.; Gao, Y.; Sun, H. L.; Zhou, S. B. A Bio-Inspired Rod-Shaped Nanoplatform for Strongly Infecting Tumor Cells and Enhancing the Delivery Efficiency of Anticancer Drugs. *Adv. Funct. Mater.* **2016**, *26*, 66−79.

(25) Huang, X. L.; Teng, X.; Chen, D.; Tang, F. Q.; He, J. Q. The Effect of the Shape of Mesoporous Silica Nanoparticles on Cellular Uptake and Cell Function. *Biomaterials* **2010**, *31*, 438−448.

DOI: 10.1021/acsnano.7b00216
ACS Nano XXXX, XXX, XXX−XXX

(26) Alemdaroglu, F. E.; Alemdaroglu, N. C.; Langguth, P.; Herrmann, A. Cellular Uptake of DNA Block Copolymer Micelles with Different Shapes. *Macromol. Rapid Commun.* **2008**, *29*, 326−329.
(27) Sun, C. Y.; Shen, S.; Xu, C. F.; Li, H. J.; Liu, Y.; Cao, Z. T.; Yang, X. Z.; Xia, J. X.; Wang, J. Tumor Acidity-Sensitive Polymeric Vector for Active Targeted siRNA Delivery. *J. Am. Chem. Soc.* **2015**, *137*, 15217−15224.
(28) Han, K.; Zhang, W. Y.; Zhang, J.; Lei, Q.; Wang, S. B.; Liu, J. W.; Zhang, X. Z.; Han, H. Y. Acidity-Triggered Tumor-Targeted Chimeric Peptide for Enhanced Intra-Nuclear Photodynamic Therapy. *Adv. Funct. Mater.* **2016**, *26*, 4351−4361.
(29) Tannock, I. F.; Rotin, D. Acid pH in Tumors and Its Potential for Therapeutic Exploitation. *Cancer Res.* **1989**, *49*, 4373−4384.
(30) Wen, Y.; Roudebush, S. L.; Buckholtz, G. A.; Goehring, T. R.; Giannoukakis, N.; Gawalt, E. S.; Meng, W. S. Coassembly of Amphiphilic Peptide EAK16-II with Histidinylated Analogues and Implications for Functionalization of β-Sheet Fibrils. *Biomaterials* **2014**, *35*, 5196−5205.
(31) Wang, M.; Adikane, H. V.; Duhamel, J.; Chen, P. Protection of Oligodeoxynucleotides Against Nuclease Degradation Through Association with Self-Assembling Peptides. *Biomaterials* **2008**, *29*, 1099−1108.
(32) Feng, T.; Ai, X. Z.; An, G. H.; Yang, P. P.; Zhao, Y. L. Charge-Convertible Carbon Dots for Imaging-Guided Drug Delivery with Enhanced *in Vivo* Cancer Therapeutic Efficiency. *ACS Nano* **2016**, *10*, 4410−4420.
(33) Han, S. S.; Li, Z. Y.; Zhu, J. Y.; Han, K.; Zeng, Z. Y.; Hong, W.; Li, W. X.; Jia, H. Z.; Liu, Y.; Zhang, X. Z.; et al. Dual-pH Sensitive Charge-Reversal Polypeptide Micelles for Tumor-Triggered Targeting Uptake and Nuclear Drug Delivery. *Small* **2015**, *11*, 2543−2554.
(34) Bobe, S. R.; Al Kobaisi, M.; Bhosale, S. V.; Bhosale, S. V. Solvent-Tuned Self-Assembled Nanostructures of Chiral l/d-Phenylalanine Derivatives of Protoporphyrin IX. *ChemistryOpen* **2015**, *4*, 516−522.
(35) Bhosale, S. V.; Kalyankar, M. B.; Bhosale, S. V.; Patil, S. G.; Lalander, C. H.; Langford, S. J.; Nalage, S. V. Supramolecular Self-assembly of Protoporphyrin IX Amphiphiles into Worm-like and Particular Aggregates. *Supramol. Chem.* **2011**, *23*, 263−268.
(36) Lee, D. J.; Oh, Y. T.; Lee, E. S. Surface Charge Switching Nanoparticles for Magnetic Resonance Imaging. *Int. J. Pharm.* **2014**, *471*, 127−134.
(37) Wen, Y.; Roudebush, S. L.; Buckholtz, G. A.; Goehring, T. R.; Giannoukakis, N.; Gawalt, E. S.; Meng, W. S. Coassembly of Amphiphilic Peptide EAK16-II with Histidinylated Analogues and Implications for Functionalization of β-sheet Fibrils. *Biomaterials* **2014**, *35*, 5196−5205.
(38) Han, K.; Liu, Y.; Yin, W. N.; Wang, S. B.; Xu, Q.; Zhuo, R. X.; Zhang, X. Z. A FRET-Based Dual-Targeting Theranostic Chimeric Peptide for Tumor Therapy and Real-time Apoptosis Imaging. *Adv. Healthcare Mater.* **2014**, *3*, 1765−1768.
(39) Cardone, R. A.; Casavola, V.; Reshkin, S. J. The Role of Disturbed pH Dynamics and The Na^+/H^+ Exchanger in Metastasis. *Nat. Rev. Cancer* **2005**, *5*, 786−795.
(40) Agarwal, R.; Singh, V.; Jurney, P.; Shi, L.; Sreenivasan, S. V.; Roy, K. Mammalian Cells Preferentially Internalize Hydrogel Nanodiscs Over Nanorods and Use Shape-Specific Uptake Mechanisms. *Proc. Natl. Acad. Sci. U. S. A.* **2013**, *110*, 17247−17252.
(41) Meng, H.; Yang, S.; Li, Z. X.; Xia, T.; Chen, J.; Ji, Z. X.; Zhang, H. Y.; Wang, X.; Lin, S. J.; Nel, A. E.; et al. Aspect Ratio Determines the Quantity of Mesoporous Silica Nanoparticle Uptake by a Small GTPase-Dependent Macropinocytosis Mechanism. *ACS Nano* **2011**, *5*, 4434−4447.
(42) Chen, J. R.; Clay, N. E.; Park, N. H.; Kong, H. Non-Spherical Particles for Targeted Drug Delivery. *Chem. Eng. Sci.* **2015**, *125*, 20−24.
(43) Sangabathuni, S.; Murth, R. V.; Chaudhary, P. M.; Surve, M.; Banerjee, A.; Kikkeri, R. Glyco-Gold Nanoparticle Shapes Enhance Carbohydrate-Protein Interactions in Mammalian Cells. *Nanoscale* **2016**, *8*, 12729−12735.
(44) Chen, S. F.; Cao, Z. Q.; Jiang, S. Y. Ultra-Low Fouling Peptide Surfaces Derived from Natural Amino Acids. *Biomaterials* **2009**, *30*, 5892−5896.
(45) Cui, J. W.; Ju, Y.; Liang, K.; Ejima, H.; Lörcher, S.; Gause, K. T.; Richardson, J. J.; Caruso, F. Nanoscale Engineering of Low-Fouling Surfaces Through Polydopamine Immobilisation of Zwitterionic Peptides. *Soft Matter* **2014**, *10*, 2656−2663.
(46) Ulijn, R. V.; Smith, A. M. Designing Peptide based Nanomaterials. *Chem. Soc. Rev.* **2008**, *37*, 664−675.
(47) Gao, Y.; Shi, J.; Yuan, D.; Xu, B. Imaging Enzyme-Triggered Self-Assembly of Small Molecules Inside Live Cells. *Nat. Commun.* **2012**, *3*, 1033−1041.
(48) Huang, P.; Wang, D. L.; Su, Y.; Huang, W.; Zhou, Y. F.; Cui, D. X.; Zhu, X. Y.; Yan, D. Y. Combination of Small Molecule Prodrug and Nanodrug Delivery: Amphiphilic Drug-Drug Conjugate for Cancer Therapy. *J. Am. Chem. Soc.* **2014**, *136*, 11748−11756.
(49) Black, K. C. L.; Wang, Y.; Luehmann, H. P.; Cai, X.; Xing, W.; Pang, B.; Zhao, Y. F.; Cutler, C. S.; Wang, L. V.; Xia, Y. N.; et al. Radioactive ^{198}Au-Doped Nanostructures with Different Shapes for *In Vivo* Analyses of Their Biodistribution, Tumor Uptake, and Intratumoral Distribution. *ACS Nano* **2014**, *8*, 4385−4394.
(50) Han, K.; Lei, Q.; Jia, H. Z.; Wang, S. B.; Yin, W. N.; Chen, W. H.; Cheng, S. X.; Zhang, X. Z. A Tumor Targeted Chimeric Peptide for Synergistic Endosomal Escape and Therapy by Dual-Stage Light Manipulation. *Adv. Funct. Mater.* **2015**, *25*, 1248−1257.
(51) Yang, G. B.; Sun, X. Q.; Liu, J. J.; Feng, L. Z.; Liu, Z. Light-Responsive, Singlet Oxygen-Triggered On-Demand Drug Release from Photosensitizer-Doped Mesoporous Silica Nanorods for Cancer Combination Therapy. *Adv. Funct. Mater.* **2016**, *26*, 4722−4732.
(52) Han, K.; Lei, Q.; Wang, S. B.; Hu, J. J.; Qiu, W. X.; Zhu, J. Y.; Yin, W. N.; Luo, X.; Zhang, X. Z. Dual-Stage-Light-Guided Tumor Inhibition by Mitochondria-Targeted Photodynamic Therapy. *Adv. Funct. Mater.* **2015**, *25*, 2961−2971.
(53) Cheng, H.; Zhu, J. Y.; Xu, X. D.; Qiu, W. X.; Lei, Q.; Han, K.; Cheng, Y. J.; Zhang, X. Z. Activable Cell-Penetrating Peptide Conjugated Prodrug for Tumor Targeted Drug Delivery. *ACS Appl. Mater. Interfaces* **2015**, *7*, 16061−16069.
(54) Kelson, M. M. A.; Bhosale, R. S.; Ohkubo, K.; Jones, L. A.; Bhosale, S. V.; Gupta, A.; Fukuzumi, S.; Bhosale, S. V. A Simple Zinc-Porphyrin-NDI Dyad System Generates a Light Energy to Proton Potential Across a Lipid Membrane. *Dyes Pigm.* **2015**, *120*, 340−346.

DOI: 10.1021/acsnano.7b00216
ACS Nano XXXX, XXX, XXX−XXX